Semiconductor Science and Technology

PAPER • **OPEN ACCESS**

Characterization of solution-grown and sputtered $In_x(O,S)_y$ buffer layers in $Cu(In,Ga)Se_2$ solar cells by analytical TEM

To cite this article: Xiaowei Jin *et al* 2020 *Semicond. Sci. Technol.* **35** 034001

OPEN ACCESS
IOP Publishing
Semiconductor Science and Technology
Semicond. Sci. Technol. **35** (2020) 034001 (7pp)
https://doi.org/10.1088/1361-6641/ab6159

Characterization of solution-grown and sputtered $In_x(O,S)_y$ buffer layers in $Cu(In,Ga)Se_2$ solar cells by analytical TEM

Xiaowei Jin[1], Reinhard Schneider[1], Radian Popescu[1], Dimitrios Hariskos[2], Wolfram Witte[2], Michael Powalla[2] and Dagmar Gerthsen[1]

[1] Laboratory for Electron Microscopy, Karlsruhe Institute of Technology (KIT), Engesserstr. 7, D-76131, Karlsruhe, Germany
[2] Zentrum für Sonnenenergie- und Wasserstoff-Forschung Baden-Württemberg (ZSW), Meitnerstr. 1, D-70563, Stuttgart, Germany

E-mail: xiaowei.jin@kit.edu

Received 18 August 2019, revised 23 October 2019
Accepted for publication 12 December 2019
Published 29 January 2020

Abstract

$Cu(In,Ga)Se_2$ thin-film solar cells were fabricated with $In_x(O,S)_y$ as buffer material, where the buffer was deposited by either solution growth or radio-frequency sputtering. To elucidate the influence of the particular deposition technique on the properties of the $In_x(O,S)_y$ layers, their structural peculiarities were characterized by high-resolution transmission electron microscopy (TEM) and nanobeam electron diffraction. Energy-dispersive x-ray spectroscopy in combination with scanning TEM was used for chemical analysis of the interfacial regions between $Cu(In,Ga)Se_2$ absorber and $In_x(O,S)_y$ layer as well as of the buffer itself. In general, the solution-grown and sputtered $In_x(O,S)_y$ layers show a nanocrystalline structure. In both types of $In_x(O,S)_y$ buffer layers, crystalline phases of tetragonal In_2S_3 and cubic In_2O_3 were detected. In addition, there are hints for the formation of a Cu-containing phase, e.g. hexagonal CuS in the sputtered $In_x(O,S)_y$ layer. Moreover, there are also distinct differences in the chemical composition of the two analyzed $In_x(O,S)_y$ layers, namely in the solution-grown $In_x(O,S)_y$ buffer layer the oxygen content is considerably higher than in the sputtered $In_x(O,S)_y$ layer.

Keywords: thin-film solar cell, $Cu(In,Ga)Se_2$, $In_x(O,S)_y$ buffer, transmission electron microscopy, energy-dispersive x-ray spectroscopy

(Some figures may appear in colour only in the online journal)

1. Introduction

Thin-film solar cells with chalcopyrite-type absorbers based on $Cu(In,Ga)Se_2$ (CIGSe) or $Cu(In,Ga)(S,Se)_2$ are widely used and exhibit power-conversion efficiencies well above 22% [1, 2]. Often chalcopyrite-type solar cells comprise a stack of a CIGSe absorber with a CdS buffer, i-ZnO, and ZnO:Al window layer deposited on a Mo back contact with soda-lime glass substrate. Usually, the CdS buffer layers on CIGSe are prepared by chemical bath deposition (CBD), yielding solar cells and modules with the highest and most reproducible efficiencies. In addition to CBD further deposition techniques like atomic layer deposition, ion-layer gas reaction, evaporation, sputtering, and spray deposition can be employed to grow thin buffer layers on chalcopyrite-type absorbers (see, e.g. [3–6]). Usually CBD is a relatively simple deposition route, yielding a reasonably good film quality and surface/step coverage (see, e.g. [7]). However, the use of CBD to grow sulfide buffers always results in films

containing more or less hydroxides and/or oxides [8], leading therefore to an unsatisfying controllability of the chemical composition, which is disadvantageous besides the generation of a high quantity of liquid waste and air exposure of CIGSe absorbers by breaking the vacuum. From a technical point of view a 'dry' and in-line or roll-to-roll compatible process such as sputtering would be favorable.

For CIGSe-based solar cells, there is an increasing interest to replace the widely used CdS buffers by Cd-free materials because of environmental reasons and the fact that the CdS with a bandgap energy of about 2.4–2.5 eV limits the level of optimum cell performance due to parasitic light absorption (see, e.g. [3, 9]). In this context, $In_x(O,S)_y$ with a tunable bandgap energy between 2.0 and 3.0 eV [10] has become a promising candidate among other possible materials, e.g. Zn(O,S) and (Zn,Mg)O (see [3, 4, 9]). In this work, $In_x(O,S)_y$ buffer layers were prepared on polycrystalline CIGSe by either CBD or radio-frequency magnetron sputtering. The microstructure of the two different $In_x(O,S)_y$ layers and the corresponding CIGSe/buffer interfaces was studied by high-resolution transmission electron microscopy (HRTEM) and nanobeam electron diffraction (NBD) on complete devices. Chemical analyses of the differently grown $In_x(O,S)_y$ buffers and their interfaces to the adjacent CIGSe absorber were performed by combined scanning transmission electron microscopy (STEM) and energy-dispersive x-ray spectroscopy (EDXS).

2. Methods

The CIGSe solar cells investigated in this study consist of a soda-lime glass substrate, a sputtered Mo back contact, a CIGSe absorber, an $In_x(O,S)_y$ buffer layer (grown by either CBD or sputtering), rf-sputtered i-ZnO, dc-sputtered ZnO:Al front contact, and Ni-Al grid fingers on top. The total cell area is 0.5 cm^2 and the cells were not covered by anti-reflective coating. The CIGSe absorbers were deposited by means of in-line multi-stage co-evaporation [11]. For both types of solar cells, the absorbers had a [Ga]/([Ga]+[In]) ratio of approximately 0.3 and a [Cu]/([Ga]+[In]) ratio of 0.85 as determined by x-ray fluorescence measurements. The CIGSe absorbers were not treated by alkali-metal salt post deposition prior to buffer deposition. The nominal thickness of the solution-grown and the sputtered $In_x(O,S)_y$ buffer is 20 nm and 60 nm, respectively. The growth of the CBD-$In_x(O,S)_y$ was carried out in acidic solution at pH $\sim$ 3.3 by reaction of $InCl_3$ (5 mM) and thioacetamide (15 mM) as organosulfide [12, 13]. In addition, small amounts of citric acid ($\sim$2 mM) were added in the solution as chelating agent to better control the growth kinetics. The deposition temperature of the CBD-$In_x(O,S)_y$ was 80 °C. In a second experimental campaign, $In_x(O,S)_y$ layers were deposited on CIGSe by rf-magnetron sputtering in static mode in a von Ardenne lab coater at a substrate temperature of 220 °C. A commercially available sintered $In_2(O_{0.25}S_{0.75})_3$ target with a diameter of 20 cm was used. The deposition was performed in pure Ar as sputtering gas (no oxygen was added). The as-grown CIGSe solar cells without light-soaking or post-annealing procedures were analyzed by a WACOM AM1.5G solar simulator with four point geometry at standard testing conditions. X-ray diffraction (XRD) measurements were carried out with a PANalytical Empyrian with Cu K_α radiation in Bragg–Brentano geometry.

To characterize the CIGSe solar cells by transmission electron microscopy (TEM), cross-sectional TEM specimens were prepared by focused ion beam (FIB) milling by an FEI Helios G4 dual-beam microscope. The FIB lamellae were mounted on Si Omniprobe lift-out grids (Cu-free) and were finally polished by a Ga^+-ion beam with a low energy of 1 keV. HRTEM images and NBD patterns (approximately 8 nm probe diameter) were acquired by an image-aberration corrected FEI Titan^3 80–300 transmission electron microscope operated at 300 kV. EDXS mapping was performed on an FEI Tecnai Osiris transmission electron microscope at 200 kV with an FEI ChemiSTEM energy-dispersive x-ray detector, where STEM high-angle annular dark-field (HAADF) images were acquired simultaneously. The EDXS data were recorded and quantified by the Esprit software of Bruker, and the semi-quantification was carried out by the thin-foil approximation [14]. The recorded NBD patterns were evaluated by calculating the azimuthally integrated intensities (2π integral) along the spatial frequency k in the initial pattern. Structure analysis was performed using the whole-diffraction-pattern fitting procedure to determine the position of each diffraction line as a function of k after background subtraction by fitting a Voigt function to each individual profile. To analyze the structure of possible crystalline phases, the resulting intensity profile was then compared with diffraction intensities calculated for known phases by using the JEMS program package [15].

3. Results and discussion

For the solar cell with CBD-$In_x(O,S)_y$ buffer a power-conversion efficiency of 14.6% was recorded, whereas that of the cell with sputtered $In_x(O,S)_y$ amounted to 13.5%, mainly due to a reduced open-circuit voltage of 594 mV compared to 645 mV for the cell with solution-grown buffer. XRD patterns (not shown here) obtained on 300 nm (CBD) and 500 nm (sputtering) thick $In_x(O,S)_y$ layers directly deposited on glass or molybdenum/glass substrates revealed an x-ray amorphous structure for both, sputtered and solution-grown layers.

As to the solar cell with CBD-$In_x(O,S)_y$ buffer layer, typical microchemical properties obtained by combined STEM/EDXS are depicted in figure 1. Figure 1(a) shows a STEM HAADF image of the CIGSe/CBD-$In_x(O,S)_y$/i-ZnO/ZnO:Al interfacial region, where each layer shows different contrast. The surface of the CIGSe absorber is very rough, leading to a corresponding uneven course of the CBD-$In_x(O,S)_y$/i-ZnO/ZnO:Al layers on top. A comparatively plane CIGSe/CBD-$In_x(O,S)_y$/i-ZnO interfacial region was selected for EDXS analyses, as indicated by a red arrow. The corresponding x-ray intensity line profile is presented in figure 1(b). In the line profile, the x-ray intensity of each element is drawn as a function of the

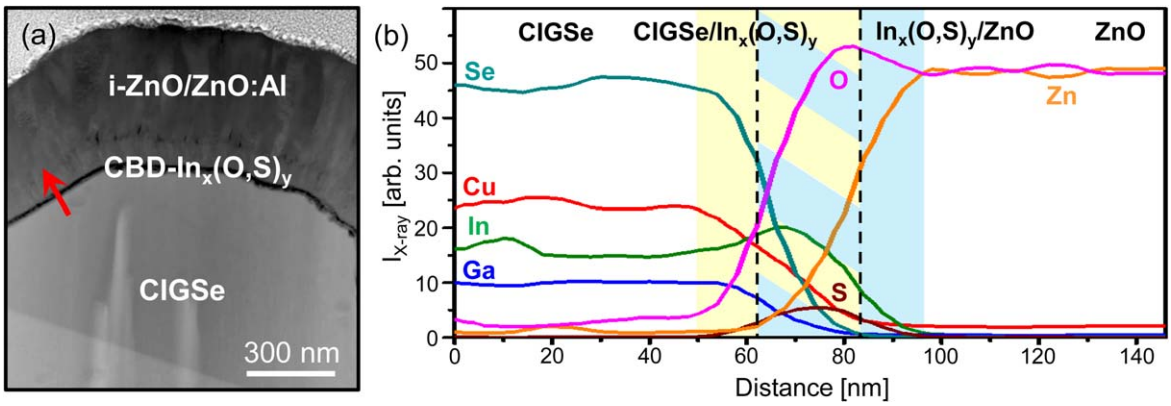

Figure 1. (a) Cross-sectional high-angle annular dark-field image of a Cu(In,Ga)Se_2/solution-grown $In_x(O,S)_y$/i-ZnO/ZnO:Al interfacial region; (b) x-ray intensities of the elements Cu (red), In (green), Ga (blue), Se (turquois), S (brown), O (pink) and Zn (orange) as a function of position across the absorber/buffer transition denoted by a red arrow in (a). The inclined Cu(In,Ga)Se_2/solution-grown $In_x(O,S)_y$ interface is marked in yellow, the inclined solution-grown $In_x(O,S)_y$/i-ZnO interface in light blue, and the overlap region between the two inclined interfaces along the electron beam direction by a yellow/blue pattern.

position along the arrow (see figure 1(a)). From the course of the individual element-intensity curves one can conclude that the CIGSe/CBD-$In_x(O,S)_y$/i-ZnO interfaces seem to be inclined with respect to the incident electron beam. The inclined CIGSe/CBD-$In_x(O,S)_y$ interface originates at the point where one of the elements in the buffer (e.g. S) starts to increase and it ends at the point where one of the elements in the absorber (e.g. Se) reaches zero, as denoted in yellow. In a similar manner, the inclined CBD-$In_x(O,S)_y$/i-ZnO interface begins at the point where the Zn signal starts to increase and it ends at the point where one of the elements in the buffer (e.g. S) reaches zero (see light blue region). Due to the thin buffer layer (20 nm) and the large inclination angle there is an overlap region between the two inclined interfaces along the electron beam direction which is marked by a yellow/blue pattern. According to the line profile, In, O and S are detected in the buffer layer. Other elements in the buffer region are artifacts due to the above-mentioned inclined interfaces. We note that the low Cu signal in the region of the CBD-$In_x(O,S)_y$/i-ZnO interface and in the ZnO layer, where Se and Ga are absent, is supposed to be an artifact due to some artificial background level. It is difficult to determine the composition of the CBD-$In_x(O,S)_y$ buffer based on the present data, because O and In signals in the buffer are detected from the adjacent ZnO layer and CIGSe absorber, respectively, due to the inclined CIGSe/CBD-$In_x(O,S)_y$/i-ZnO interfaces. However, we detect a pronounced O signal in the CIGSe/CBD-$In_x(O,S)_y$ interface region, where Zn is absent (i.e. the influence of O from the ZnO layer is negligible), indicating that a distinct amount of O, stemming from the CBD process, is present in the buffer. We note that the low O signal in the CIGSe absorber is an artifact due to the oxidation of the FIB lamella.

Figure 2(a) depicts an HRTEM image of an interface region between CIGSe and CBD-$In_x(O,S)_y$. The interface is clearly visible due to the difference in contrast between the absorber and the buffer layer, and it is parallel to the (−112) planes of CIGSe with a tetragonal chalcopyrite structure [16]. The CBD-$In_x(O,S)_y$ layer shows a nanocrystalline structure with grain sizes below 10 nm (a typical nanocrystallite with a grain size of ∼5 nm is marked in figure 2(a)), and a defined orientation relationship is not observed between the buffer crystallites and crystal lattice of the absorber. Considering that the crystallinity of the film is strongly influenced by the orientation of the substrate due to the lattice mismatch between them, other CIGSe/CBD-$In_x(O,S)_y$ interfaces with different orientations (e.g. parallel to the (22-8) plane of CIGSe [13]), were also investigated by HRTEM imaging. Our results show that all investigated CBD-$In_x(O,S)_y$ buffer regions exhibit a nanocrystalline structure, independent of the orientation of the underlying CIGSe grains. Thus, the formation of $In_x(O,S)_y$ nanocrystallites in the solution-grown buffer can be attributed to the deposition conditions and the chosen growth route.

Due to the small thickness of the CBD-$In_x(O,S)_y$ layer, the chemical phases in the buffer were studied by NBD experiments as shown in figure 2(b). The zero-order beam of the unscattered electrons with the highest intensity is located in the center of the NBD pattern. Numerous Bragg reflections are visible at different spatial frequencies which are characteristic for the crystal structure of the phases present in the buffer layer. The NBD pattern was azimuthally integrated to obtain an intensity profile as a function of the spatial frequency k that is presented in figure 2(c). In this profile, the intensity of each reflection is background-subtracted. The EDXS results in figure 1 indicate that the phases in the buffer consist of only In, S and O. Hence, all the possible phases with known lattice parameters, such as α-In_2S_3, β-In_2S_3, γ-In_2S_3, InS, In_5S_4, In_6S_7, cubic In_2O_3, orthorhombic In_2O_3 and rhombohedral In_2O_3 were used to fit the azimuthally integrated intensity profile. The result is that α-In_2S_3 or β-In_2S_3, and cubic In_2O_3 fit the profile better than others. Moreover, it is reported that β-In_2S_3 is considerably more stable than α-In_2S_3 below 476 °C [17]. As the deposition temperature of the buffer layer was only 80 °C, the presence of β-In_2S_3 within the buffer is most likely. Thus, In_2S_3 with a tetragonal structure ($I4_1/amd$, $a = b = 7.59$ Å, $c = 32.35$ Å) [18] and In_2O_3 with a cubic bixbyite structure (Ia-3,

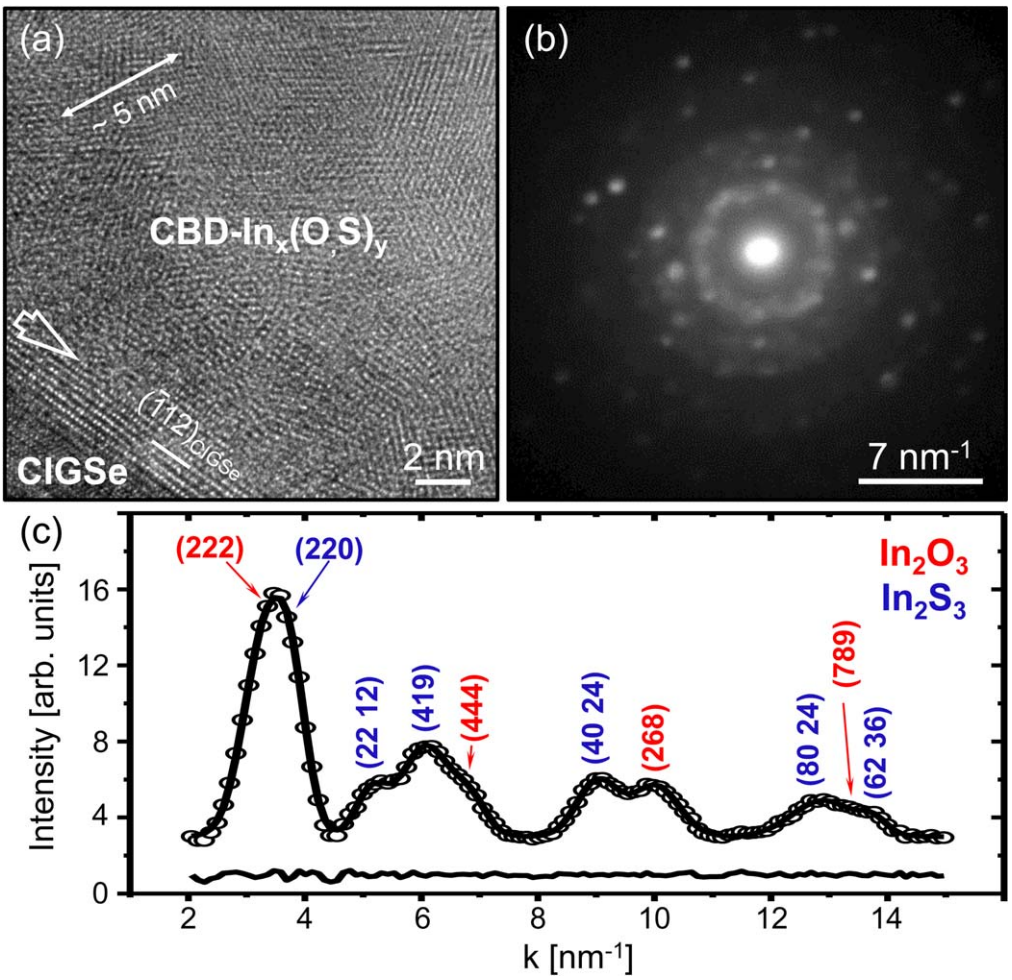

Figure 2. (a) High-resolution transmission electron microscopy image of a Cu(In,Ga)Se_2/solution-grown $In_x(O,S)_y$ interfacial region with the interface parallel to the (−112) plane of the absorber, the absorber/buffer interface is marked by a white arrow; (b) nanobeam electron diffraction pattern of the solution-grown $In_x(O,S)_y$ layer; (c) resulting azimuthally integrated intensity profile of the nanobeam electron diffraction pattern (the extra solid line represents the residual after background fit). The fit yields tetragonal In_2S_3 and cubic In_2O_3 as the most probable phases in the analyzed volume.

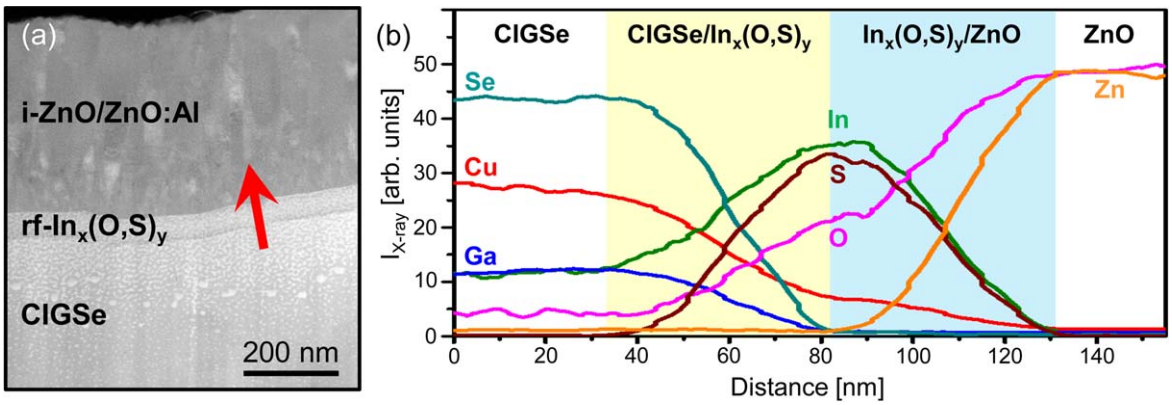

Figure 3. (a) Cross-sectional high-angle annular dark-field image of a Cu(In,Ga)Se_2/sputtered $In_x(O,S)_y$/i-ZnO/ZnO:Al interfacial region; (b) x-ray intensities of the elements Cu (red), In (green), Ga (blue), Se (turquois), S (brown), O (pink) and Zn (orange) as a function of position across the absorber/buffer transition denoted by a red arrow in (a). The inclined Cu(In,Ga)Se_2/sputtered $In_x(O,S)_y$ interface is marked by a yellow rectangle and the inclined sputtered $In_x(O,S)_y$/i-ZnO interface by a light blue rectangle.

$a = 10.12$ Å) [19] are assigned to the CBD-$In_x(O,S)_y$ layer. We note that—apart from the (220) In_2S_3 and the (222) In_2O_3 reflections—low-index Bragg reflections with large structure

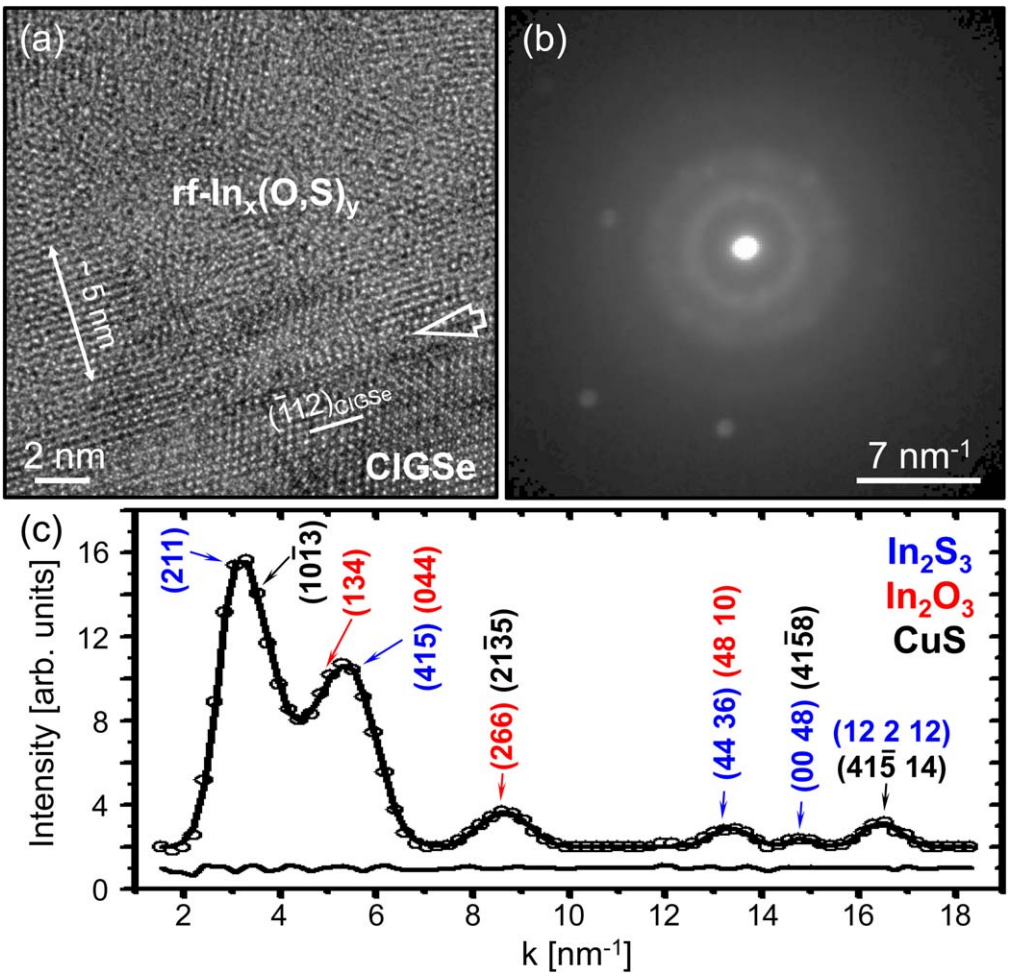

Figure 4. (a) High-resolution transmission electron microscopy image of a Cu(In,Ga)Se$_2$/sputtered In$_x$(O,S)$_y$ interfacial region with the interface parallel to the (−112) plane of the absorber, the absorber/buffer interface is marked by a white arrow; (b) nanobeam electron diffraction pattern of the sputtered In$_x$(O,S)$_y$ layer; (c) resulting azimuthally integrated intensity profile of the nanobeam electron diffraction pattern (the extra solid line is the residual after background fit). The fit yields tetragonal In$_2$S$_3$, cubic In$_2$O$_3$ and hexagonal CuS as the most probable phases in the analyzed volume.

factors are not observed in figure 2(c). This fact can be attributed to the small analyzed volume under NBD conditions which does not provide a grain ensemble with statistical orientation distribution. Moreover, the occurrence of other phases cannot be excluded due to the small analyzed volume.

For comparison, the microchemical and microstructural properties of the sputtered In$_x$(O,S)$_y$ buffer in the CIGSe solar cells were studied. Figure 3(a) shows a STEM HAADF image of a section of the CIGSe/sputtered In$_x$(O,S)$_y$/i-ZnO/ZnO:Al interface. The thickness of the sputtered In$_x$(O,S)$_y$ layer is measured to be 60 nm. Other structural peculiarities, such as the roughness of the absorber surface and the thickness of the window layer, are similar compared to those of the solar cell with CBD buffer (see figure 1(a)). A region across the CIGSe/sputtered In$_x$(O,S)$_y$/i-ZnO interfaces was chosen for EDXS analyses (red arrow in figure 3(a)). In the corresponding x-ray intensity line profile shown in figure 3(b), the projected area of the inclined CIGSe/sputtered In$_x$(O,S)$_y$ interface is marked by a yellow rectangle and the inclined sputtered In$_x$(O,S)$_y$/i-ZnO one by a light blue rectangle. No overlap region between the two inclined interfaces along the electron beam direction is observed due to the relatively thick buffer layer (60 nm). The line profile shows that besides In, O and S, Cu is also present in the buffer layer, because Cu is contained in the sputtered In$_x$(O,S)$_y$/i-ZnO interface, where Se and Ga are absent. This Cu signal is higher than the Cu background level in the ZnO layer. The chemical composition of the sputtered In$_x$(O,S)$_y$ buffer cannot be exactly determined, but the O and S intensities in the CIGSe/sputtered In$_x$(O,S)$_y$ interface, where Zn is absent (i.e. the influence of O from the ZnO layer is negligible), indicating that more S than O is present in the buffer, which is in accordance with the used S-rich target composition.

Figure 4(a) shows an HRTEM image of a CIGSe/sputtered In$_x$(O,S)$_y$ interfacial region. The interface is parallel to the (−112) planes of the chalcopyrite CIGSe, which is the same situation as for the interface shown in figure 2(a). The sputtered In$_x$(O,S)$_y$ layer is nanocrystalline with random crystallite orientation. Regions of the sputtered In$_x$(O,S)$_y$ buffers grown on other lattice planes of the CIGSe grains also show a nanocrytalline structure as for the CBD-In$_x$(O,S)$_y$ buffer. In contrast, Soni *et al* [20] found amorphous In$_2$S$_3$

layers right after sputter deposition on CIGSe at room temperature, which became nanocrystalline after annealing at 210 °C for 15 min, quite similar to the substrate temperature of 220 °C during sputtering of our $In_x(O,S)_y$ layer.

NBD experiments were also carried out to investigate the crystalline phases in the sputtered $In_x(O,S)_y$ buffer layer (figure 4(b)). Since Cu was detected in the buffer by EDXS (see figure 3(b)), possible Cu-containing phases such as CuS, Cu_2S, CuO, Cu_2O, $CuIn_5S_8$, and $CuIn_3S_5$ have to be considered to fit the spatial frequencies in the azimuthally integrated intensity profile of figure 4(c) in addition to the expected In-, S- and O-containing phases. The fit procedure shows that In_2S_3 with a tetragonal structure and In_2O_3 with a cubic structure are present. CuS with a hexagonal structure ($P6_3mc$, $a = b = 3.79$ Å, $c = 16.33$ Å) [21] is identified as the most probable Cu-containing phase. However, the presence of additional phases, especially other Cu-containing phases, cannot be excluded due to the small analyzed volume.

For oxygen-free In_xS_y buffer layers sputtered on CIGSe, Abou-Ras *et al* [22] reported that Cu, In and Ga interdiffusion occurs between absorber and buffer for substrate temperatures between 60 °C and 250 °C. This interdiffusion becomes more pronounced with increasing temperature and causes the formation of a $CuIn_5S_8$ interlayer at 340 °C, which limits the cell efficiency. In the case of our CIGSe/sputtered $In_x(O,S)_y$ system, the substrate temperature was 220 °C during sputtering of $In_x(O,S)_y$, and a distinct Cu diffusion into the buffer is discovered. This interdiffusion can explain the existence of hexagonal CuS as revealed by NBD. However, Ga or In interdiffusion was not detected for both the CBD- and sputtered $In_x(O,S)_y$ layers. In comparison, Ho *et al* [23] deposited $In_x(O,S)_y$ buffer layers on CIGSe absorbers by pulsed-DC sputtering of a pure indium sulfide target at room temperature (20 °C). For a high base pressure of 1.33×10^{-2} Pa during In_2S_3 deposition, the [O]/([O]+[S]) ratio was 0.30–0.38, similar with our results. However, by means of x-ray photoelectron spectroscopy, no Cu was detected in the $In_x(O,S)_y$ layer, even not after extra air annealing at 235 °C and 280 °C. This indicates that Cu interdiffusion does not occur between CIGSe and $In_x(O,S)_y$ for a substrate temperature of 20 °C, which is not changed by annealing at 235 °C and 280 °C.

In comparison with the CBD-$In_x(O,S)_y$ buffer, more S than O is found in the sputtered $In_x(O,S)_y$ layer, which may result from the deposition procedure by different methods, hinting at more In_2S_3 nanograins than In_2O_3 nanograins in the layer. Barreau *et al* [24] reported that the bandgap of $In_2(O,S)_3$ layers can be enlarged by increasing the O concentration, which may contribute to the higher open-circuit voltage of the cell with CBD-$In_x(O,S)_y$ compared to that with sputtered $In_x(O,S)_y$.

4. Conclusion

To find a good Cd-free material as the buffer layer of CIGSe thin-film solar cells and to optimize the cell performance, $In_x(O,S)_y$ layers were deposited on polycrystalline CIGSe by two applicable methods, i.e. CBD and magnetron sputtering, respectively. The microchemistry and the microstructure of these differently grown $In_x(O,S)_y$ layers and the CIGSe/$In_x(O,S)_y$ interfaces were analyzed by STEM/EDXS, HRTEM and NBD. More O than S was found in the CBD-$In_x(O,S)_y$ layer, while it is the opposite case for the $In_x(O,S)_y$ layer sputtered from the $In_2(O_{0.25}S_{0.75})_3$ target. Solution-grown and sputtered $In_x(O,S)_y$ layers show a nanocrystalline structure with random crystallite orientation. Different phases are detected in the two differently fabricated $In_x(O,S)_y$ layers comprising tetragonal In_2S_3 and cubic In_2O_3. In addition, a hexagonal CuS phase probably forms in the sputtered $In_x(O,S)_y$ layer due to Cu diffusion from CIGSe. This feature and different chemical compositions of the solution-grown and sputtered $In_x(O,S)_y$ buffer layers and their CIGSe/buffer interfaces might contribute, besides various other reasons like band alignment between CIGSe absorber and buffer, CIGSe surface treatment resulting in probably different surface passivation etc, to the slightly different performance of the investigated CIGSe thin-film solar cells.

Acknowledgments

We acknowledge the funding by the German Federal Ministry for Economic Affairs and Energy (BMWi) within the EFFCIS project under contract No. 0324076A (ZSW) and contract No. 0324076E (KIT). We thank the CIGSe team at ZSW for solar cell fabrication.

ORCID iDs

Xiaowei Jin https://orcid.org/0000-0002-0163-4211

References

[1] Jackson P, Wuerz R, Hariskos D, Lotter E, Witte W and Powalla M 2016 *Phys. Status Solidi RRL* **8** 583
[2] Green M A, Dunlop E D, Levi D H, Hohl-Ebinger J, Yoshita M and Ho-Baillie A W Y 2019 *Prog. Photovolt.: Res. Appl.* **27** 565
[3] Naghavi N *et al* 2010 *Prog. Photovolt.: Res. Appl.* **18** 411
[4] Mughal M A, Engelken R and Sharma R 2015 *Sol. Energy* **120** 131
[5] Bugot C, Bouttemy M, Schneider N, Etcheberry A, Lincot D and Donsanti F 2018 *J. Vac. Sci. Technol.* A **36** 061510
[6] Karthikeyan S, Hill A E and Pilkington R D 2017 *Appl. Surf. Sci.* **418** 199
[7] Gopinath G R, Miles R W and Ramakrishna Reddy K T 2013 *Energy Proc.* **34** 399
[8] Lokhande C D, Ennaoui A, Patil P S, Giersig M, Diesner K, Muller M and Tributsch H 1999 *Thin Solid Films* **340** 18
[9] Witte W, Spiering S and Hariskos D 2014 *Vak. Forsch. Prax.* **26** 23
[10] Barreau N, Bernède J C, Marsillac S and Mokrani A 2002 *J. Cryst. Growth* **235** 439
[11] Voorwinden G, Kniese R, Jackson P and Powalla M 2007 *Proc. 22nd European Photovoltaic Solar Energy Conf.* pp 2115–8

[12] Hariskos D, Ruckh M, Rühle U, Walter T, Schock H W, Hedström J and Stolt L 1996 *Sol. Energ. Mat. Sol.* C **41/42** 345
[13] Jin X, Popescu R, Pasha A, Schneider R, Hariskos D, Witte W, Powalla M and Gerthsen D 2019 *Thin Solid Films* **671** 133
[14] Cliff G and Lorimer G W 1975 *J. Microsc.* **103** 203
[15] Stadelmann P A 1987 *Ultramicroscopy* **21** 131
[16] Díaz R, Martín T, Merino J M, León M, Martín de Vidales J L and Rueda F 2000 *J. Appl. Phys.* **88** 1776
[17] Pistor P, Merino Álvarez J M, León M, Michiel M D, Schorr S, Klenk R and Lehmann S 2016 *Acta Cryst.* **B72** 410
[18] Lafond A, Rocquefelte X, Paris M, Guillot-Deudon C and Jouenne V 2011 *Chem. Mater.* **23** 5168
[19] Nadaud N, Lequeux N, Nanot M, Jové J and Roisnel T 1998 *J. Solid State Chem.* **135** 140
[20] Soni P, Raghuwanshi M, Wuerz R, Berghoff B, Knoch J, Raabe D and Cojocaru-Mirédin O 2019 *Energy Sci. Eng.* **7** 478
[21] Gotsis H J, Barnes A C and Strange P 1992 *J. Phys.: Condens. Matter* **4** 10461
[22] Abou-Ras D, Kostorz G, Hariskos D, Menner R, Powalla M, Schorr S and Tiwari A N 2009 *Thin Solid Films* **517** 2792
[23] Ho W, Hsu C, Wei S, Cai C, Huang W and Lai C 2017 *ACS Appl. Mater. Interfaces* **9** 17586
[24] Barreau N, Bernède J C, El M H, Marsillac S, Castel X and Pinel J 2002 *Solid State Commun.* **122** 445